Edge sheared flows and the dynamics of blob-filaments

J.R. Myra[1], W.M. Davis[2], D.A. D'Ippolito[1], B. LaBombard[3], D.A. Russell[1], J.L. Terry[3] and S.J. Zweben[2]

[1] Lodestar Research Corporation, Boulder, CO, USA
[2] Princeton Plasma Physics Laboratory, Princeton, NJ, USA
[3] Massachusetts Institute of Technology, Cambridge, MA, USA

Abstract

The edge and scrape-off layer (SOL) region of a tokamak plasma is considered, with emphasis on sheared flow generation and the dynamics of blob-filaments. Both numerical simulations and experimental data analysis are employed. The simulations use the fluid-based two-dimensional (2D) curvature-interchange model embedded in the SOLT code. A blob-tracking algorithm based on 2D time-resolved images from the gas puff imaging diagnostic has also been developed and applied to NSTX, Alcator C-Mod and simulation data. The algorithm is able to track the blob motion and changes in blob structure, such as elliptical deformations, that can be affected by sheared flows. Results of seeded blob simulations and quasi-steady turbulence simulations are compared with the experimental data to determine the role of plasma parameters on the blob tracks and to evaluate the exchange of momentum between the blobs and flows. The simulations are shown to reproduce many qualitative and quantitative features of the data including size, scale-length and direction of perpendicular (approximately poloidal) flows, the inferred Reynolds acceleration and residual stress, poloidal reversal of blob tracks, and blob trapping and/or ejection. Mechanisms related to blob motion, SOL currents and radial inhomogeneity are shown to be sufficient to explain the presence or absence of mean and oscillating zonal sheared flows in selected shots.

(Some figures may appear in colour only in the online journal)

1. Introduction

Sheared flows play an important role in regulating turbulence in fusion plasmas [1]. Furthermore, it has been known for some time that radial inhomogeneity provides a mechanism for sheared flow generation by the turbulence [2, 3]. To date, the vast majority of work on sheared flows and turbulence has focused either on the core plasma, or on the closed flux surface regions of the edge. Considerable progress has been made in understanding the regimes and detailed dynamics of edge turbulent interactions with flows using sophisticated numerical codes [4, 5]. Here, we consider the interaction of edge and scrape-off layer (SOL) sheared flows with coherent turbulent structures, i.e. blob-filaments [6, 7], focusing on the generation of flows, the dynamics of the blob-filaments and their mutual interaction. We define a blob-filament (or simply 'blob') to be any filamentary field-aligned structure of significantly enhanced pressure in the edge or SOL region. Because coherent structures are readily observed in the edge plasma using diagnostics such as gas puff imaging (GPI) [8–10], the present approach enables a new kind of comparison of edge turbulence theory with data.

The work is motivated by several considerations. Edge sheared flows, both mean flows and oscillating zonal flows, are believed to be important for the L–H, and H–L transitions [11–21], and an improved understanding of their role will be required for a theory-based scaling of these transitions for ITER and future devices. Theoretical work predicts that the L–H transition can be described by predator–prey models [11, 12], and some recent experimental findings have confirmed many qualitative and some quantitative aspects of the predator–prey paradigm [17–21]. Flow generation by turbulence also implies forces and torques on the plasma which are of interest for understanding bulk plasma rotation.

Another motivation comes from the behaviour of blob-filaments in the SOL. Blob generation and dynamics impact both the (near-separatrix) SOL width critical for ITER power handling in the divertor [22, 23], and the far SOL interaction with plasma-facing components, which is also an important concern. Turbulent blob interactions near the separatrix generate flows, but the subsequent motion and structure of blob-filaments is also influenced by the sheared flows that they propagate through [24–30]. In some experiments, bursty transport, Reynolds accelerations and edge flows have been shown to be linked [14, 15, 31–33] The role of blob and eddy tilting, also recently investigated in other studies [34–36], will be examined as both a theoretical mechanism and a diagnostic of Reynolds stress in particular experimental discharges.
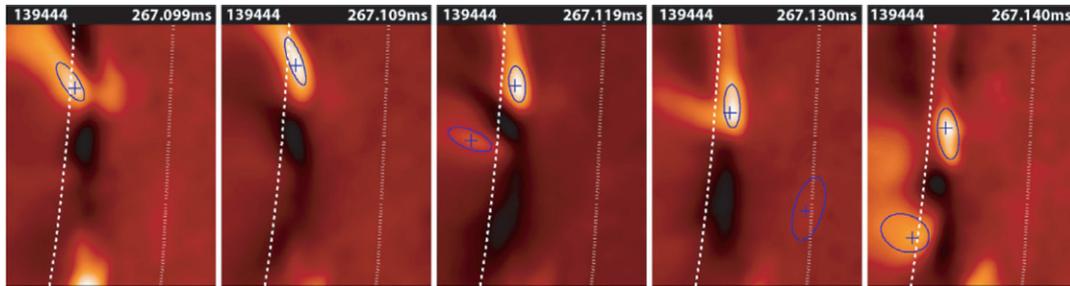
Figure 1. Normalized (see text) GPI intensity for sample frames from NSTX with the palette scaled to the maximum and minimum for each frame. The tokamak Z coordinate is vertical (approximately poloidal); R is horizontal (approximately radial). The time between illustrated frames here is $10\,\mu s$ (every fourth camera frame). The core plasma is to the left and the dashed line is the approximate (EFIT) separatrix location. The dotted line at right locates a radial limiter. The ellipses are fit by the tracking algorithm and the cross is the location of the maximum brightness within the blob. Note the overall trajectory of the bright blob and the significant elliptical distortion near the separatrix.

We will show that edge density and temperature gradients (specifically the profile of the diamagnetic velocity) and changes in edge topology at the separatrix, combined with SOL currents, are sufficiently large to explain the generation of flows observed in two experimental shots. While Reynolds stress in the presence of background sheared $E \times B$ flows leads to further flow generation, we will show that there is a symmetry-breaking effect—a natural direction for the flows in the absence of a background $E \times B$ flow. This symmetry breaking from edge profiles and SOL current flow considerations implies a residual Reynolds stress. The present mechanism is different from, and presumably acts in addition to, a magnetic-shear-induced residual Reynolds stress that has been recently investigated [37].

Unlike the core and pedestal regions of the tokamak plasma, the extreme edge and SOL regions can be subject to large ($\delta n/n \sim 1$) fluctuation levels. This presents many challenges to numerical simulations of the turbulent separatrix region, and as a result existing numerical models are not as far advanced in terms of physics content as their counterparts further into the core. The simulation model employed here has many caveats, such as cold ions, model two-dimensional (2D) geometry, fluid theory, electrostatics and the use of a simplified drift-wave physics model. Some refinements to specific aspects of this basic model have been investigated. Fluid modelling in three dimensions and some comparison with experiments has been carried out in a few works [10, 38–41] and gyrofluid modelling of the SOL has been possible in a δf quasi-local limit [42], but except for a few cases [38, 40], neither the fluid or gyrofluid efforts have been able to incorporate X-point geometry in work that compares with tokamak experimental data. In general, it becomes increasingly challenging to simulate the strong order unity fluctuations characteristic of SOL turbulence in models with greater physics fidelity or geometrical complexity.

The simulations in this paper are carried out with the SOLT code [43]. SOLT and other somewhat similar 2D electrostatic models such as ESEL [44], TOKAM2D [45] and FDET [46] have been used to study the basic dynamics of blob formation, ejection and propagation and other general features of strongly nonlinear SOL turbulence. There is by now a considerable literature on this subject and the interested reader is referred to recent reviews [6, 7] for a more complete discussion of the many works that have contributed to present understanding. One of the important applications of such codes has been

the task of modelling basic features of tokamak edge and SOL turbulence. While the 2D models are in many respects highly simplified, lacking both electromagnetic and three-dimensional (3D) geometry effects (topics which we will return to), significant points of agreement with tokamak experiments on TCV [47], NSTX [48, 49], Alcator C-Mod [50], JET [51], MAST [52] and linear machines such as TORPEX [30] and CSDX [53] have nevertheless been achieved.

Our study of the origin of sheared flow generation and its relation to blob-filament dynamics is greatly facilitated by a new analysis tool for tracking the motion and changes in structure of blobs, namely, a blob-tracking algorithm [54] based on 2D time-resolved images from the GPI diagnostic. This tool and sample results are discussed in section 2. In section 3 we consider some mechanisms for the generation of flows that are related to blob motion, SOL currents and radial inhomogeneity. The SOLT code simulation model and simulation method are described in section 4 together with the results of seeded blob and turbulence simulations for parameters relevant to NSTX and Alcator C-Mod shots. A detailed quantitative comparison of model results with experimental results is given. We also discuss the elliptical deformation of blob structures and a resulting proxy for the Reynolds stress. The net force on the tokamak plasma due to the turbulent momentum escaping across the separatrix is also considered. Finally, our conclusions are given in section 5.

2. Experimental diagnostics and analysis methods

GPI is a valuable diagnostic for the detection of edge turbulent structures and the analysis of their motion. A detailed description of the diagnostic is given elsewhere [8–10]. The basic idea is that a small amount of neutral gas (usually deuterium or helium) is puffed into the edge plasma at a particular toroidal location. The line emission from the gas, which depends on the local plasma density and temperature, is then detected and recorded by a high framing rate camera. In the present study, the camera is positioned to view the motion of the turbulent structures in the plane perpendicular to the magnetic field B. In the present datasets, a 64×64 pixel GPI image frame was captured every $2.5\,\mu s$ for a total of 20 ms.

A sequence of sample processed frames from NSTX is shown in figure 1 for the normalized GPI intensity, i.e. the local intensity $I(x, y, t)$ normalized to the time-averaged intensity

Table 1. Experimental parameters for the NSTX and Alcator C-Mod shots analysed in this paper. Values are quoted at the outboard midplane. Note especially the large difference in collisionality Λ.

	NSTX, Shot 139444	C-MOD, Shot 1100824017
$n_{e,sep}$ (m^{-3})	5.8×10^{18}	1.0×10^{20}
$T_{e,sep}$ (eV)	19	47
R (cm)	150	89
B_{sep} (T)	0.25	3.9
c_s (cm s^{-1})	3.0×10^6	4.8×10^6
Ω_i (s^{-1})	1.2×10^7	1.9×10^8
$\rho_{s,sep}$ (cm)	0.26	0.025
$\Lambda_{SOL} \sim \nu_{e*}(m_e/m_i)^{1/2}$	0.3–0.8	1–3
Blob size $\delta_{b,sep}$ (cm)	2.2 ± 0.5	0.4 ± 0.1
$\delta I/\langle I \rangle|_{sep}$	<1.6	<0.6
GPI gas	D	He
GPI imaging area (cm^2)	25×30	5.9×5.9

$\langle I(x,y) \rangle_t$. In figure 1 the time interval used for the preceding average was 10 ms. For each local maximum in the frame meeting specified filtering criteria, an ellipse is fit to the half-maximum contour level. The motion of the central maximum and changes in the elliptical fit are tracked from frame to frame [54]. The allowed displacement of a given turbulent structure between frames is restricted (typically to 10 pixels) to distinguish different structures. The structure is considered to be a blob if it meets these criteria and has a sufficient lifetime (typically taken as more than $25\,\mu s$). Note that this rather general definition of a blob can include wave crests inside the separatrix as well as isolated filamentary structures that have been ejected into the SOL.

In this paper we analyse two shots from the NSTX and Alcator C-Mod experiments. Parameters for these discharges are given in table 1. Both are ohmic plasmas; the NSTX case is preheated by neutral beams. Of particular note is the difference in the SOL collisionality parameter [7] $\Lambda = \nu_{ei}L_{||}/(\Omega_e\rho_s)$, a point to which we will return. A set of superimposed blob tracks from 3 ms of GPI data in NSTX is shown in figure 2. The fitted ellipses (starting one filled) are drawn with the same minor radius regardless of blob size (for visual clarity) and only a portion of the approximately $25 \times 30\,cm^2$ camera image is shown. The separatrix position is shown by a dashed line. Some blob tracks show outward motion (ejection), some are confined to the edge region (here defined as inside the separatrix). The motion of the edge structures is upwards, which corresponds to the electron diamagnetic direction. Some blob tracks show reversal of the poloidal (approximately vertical) velocity near the separatrix indicating the action of a downward accelerating force. The dominant motion in the SOL is downward, in the ion diamagnetic direction. One of the main goals of this paper is to understand and quantify the mechanisms responsible for the observed blob motion in the y (binormal, approximately poloidal) direction, i.e. the origin of perpendicular sheared flows.

3. Mechanisms for blob motion and sheared flow generation

Blob motion is controlled by polarization charges. The basic outward motion results from grad-B and curvature drifts which charge polarize the blob and cause it to $\boldsymbol{E} \times \boldsymbol{B}$ drift [6, 7] as
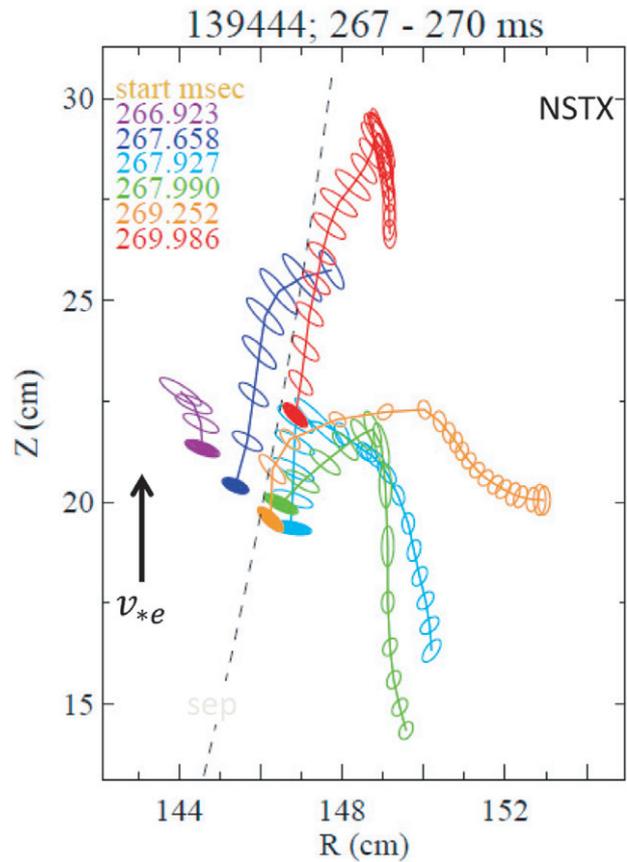

Figure 2. Superposition of selected NSTX blob tracks collected in a 3 ms time interval. All the indicated tracks start in a small region near the filled ellipses. Start times for each track are given in the inset. The electron diamagnetic drift direction is up, and the EFIT separatrix is shown with a dashed line.

illustrated in figure 3(a). Background flows or drifts can rotate and shear the blob charge dipole, converting radial motion to partly poloidal motion [55]; see figure 3(b). If there is a net monopole component to the charge or vorticity, then this implies blob rotation, figure 3(c), which when superimposed on the basic dipole also gives rise to dipole rotation. A monopole component can arise for a number of reasons. One is that currents flow to sheaths in the SOL, figure 3(d), to neutralize the blob charge dipole, and excess electrons are lost more easily than excess ions. This is due to the asymmetry of the sheath current–voltage relation.

In general, strong radial inhomogeneity present in the edge and SOL region of a tokamak plasma leads to many mechanisms for sheared flow generation and its interaction with turbulence. These mechanisms are all related to shearing and rotation or tilting deformations of the turbulent structures (called 'blobs' here both inside and outside the separatrix). The primary mechanisms can be enumerated as follows:

(1) radial variation of the wave group velocity [2, 3] on the scale of the blob radius due to steep profiles and or rapid changes in topology across the separatrix which shear and rotate the blob charge dipole, converting radial blob motion into poloidal motion;

(2) a net monopole blob potential due to adiabatic electron physics ($\delta n \sim \delta\Phi$) which induces rotation of the blob
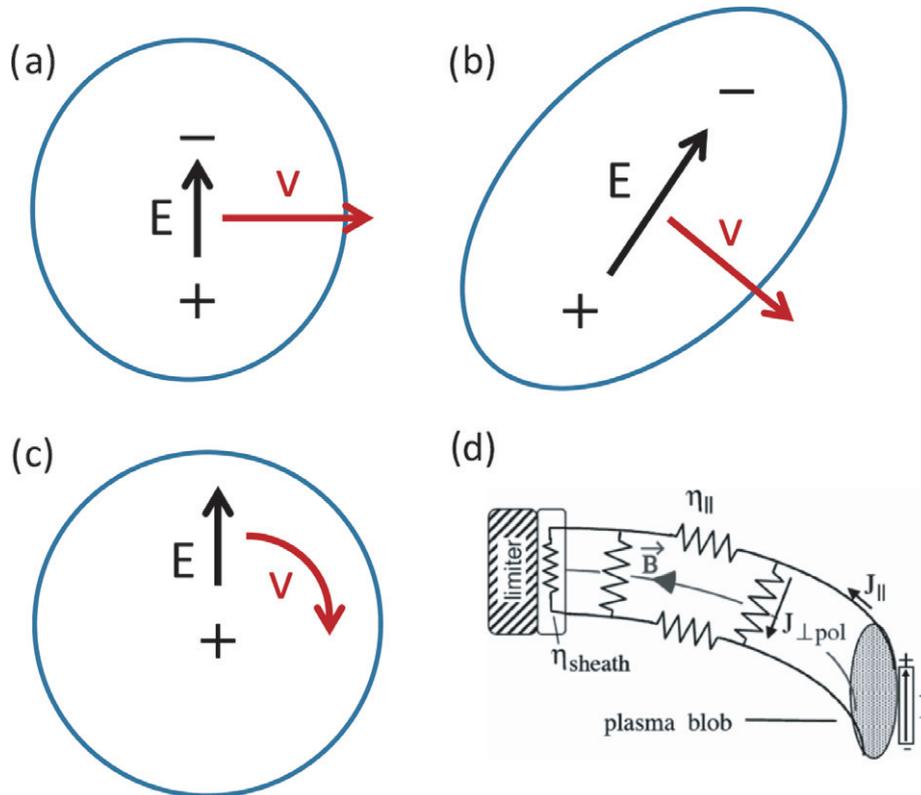
3

Figure 3. Schematic of mechanisms governing blob motion and blob generation of flows.

charge dipole [41], mixing radial and poloidal blob motion;

(3) asymmetry in the positive and negative parallel currents in the SOL (due to the asymmetry of the sheath current–voltage relation) which causes the blob to charge positive and partially rotate, again converting radial motion into poloidal motion [56];

(4) in the SOL, blob rotation for a sheath-connected filament due to finite blob T_e which induces an internal blob radial electric field [26];

(5) interaction of the blob with an existing strong $E \times B$ shear layer leading to vortex merging and charge dynamics: positive and negative regions of the blob charge dipole are repelled or attracted by regions of vorticity (charge) in the shear layer.

Some of these mechanisms have well-known counterparts in traditional nonlinear Fourier-wave theory [2, 3], but it is illuminating to see them at play in the context of coherent blob structures. Moreover, blob structures are readily detectable by the GPI diagnostic enabling an entirely new kind of comparison between theory and experiment. The five mechanisms listed above are included in the SOLT code simulations which are described next.

4. Simulations and comparison with experiment

4.1. Simulation model and Reynolds stress analysis

Simulations described in this paper were carried out with the Scrape-Off-Layer Turbulence (SOLT) code [43]. SOLT is a fluid code that models turbulence in the 2D plane (x, y) perpendicular to the magnetic field $B = Be_z$ at the outboard midplane of the torus. Here $x = \Delta r$ is radial distance measured from the separatrix, and y is binormal (approximately poloidal). SOLT implements parallel physics using closure relations [6, 49] for the midplane parallel current and parallel fluxes of particles and energy for collisional regimes ranging from sheath-connected to conduction limited. (The parallel closure relations, discussed further in appendix A, describe parallel currents and heat fluxes in the Braginskii model [57] together with sonic flow of particles to the sheath, with current and energy flux matching conditions [58] at the sheath entrance. Neoclassical and kinetic effects on the parallel dynamics are neglected). The SOLT code can describe arbitrarily strong nonlinear plasma dynamics ($\delta n/n \sim 1$), including blob formation, and the physics model supports interchange-type curvature-driven modes, sheath and Kelvin-Helmholtz instabilities, and drift waves. Details of the SOLT model have been discussed elsewhere and are summarized in appendix A. The present version assumes cold ions. SOLT also includes the self-consistent evolution of zonal (i.e. poloidally averaged) flows. For comparison with experimental GPI data, SOLT employs a synthetic GPI diagnostic to simulate both He and D gas puffs.

SOLT was used for both seeded blob simulations and quasi-steady turbulence simulations of the NSTX and Alcator C-Mod shots. The seeded blob simulations were run as SOLT initial value problems. Smoothed experimental plasma profiles of density and temperature, shown in figure 4, were employed together with other machine parameters that enter the SOLT model: magnetic field B, major radius R and connection
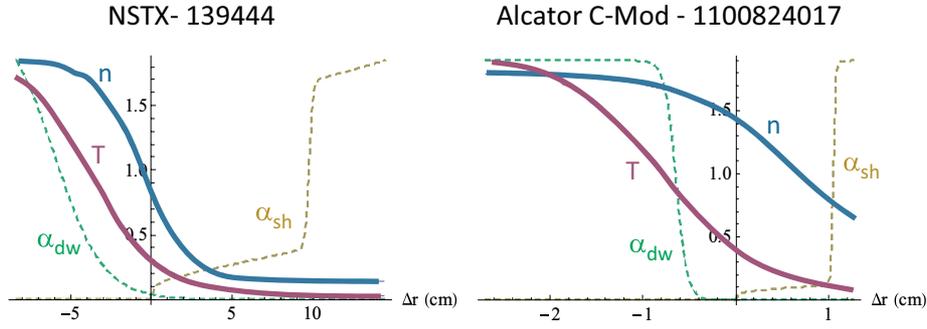
Figure 4. Smoothed normalized background profiles at the outboard midplane of density n and electron temperature T, employed in the SOLT code simulations of the shots described in table 1. Here the reference (normalization) values for NSTX are $n_0 = 7.0 \times 10^{12}$ cm^{-3} and $T_0 = 60$ eV; for C-Mod they are $n_0 = 7.3 \times 10^{13}$ cm^{-3} and $T_0 = 115$ eV. Also shown in dashed lines are the spatial variation of the normalized electron adiabaticity parameter $\alpha_{\rm dw}$ in the edge and the normalized sheath conductivity $\alpha_{\rm sh}$ in the SOL (see appendix A for definitions).
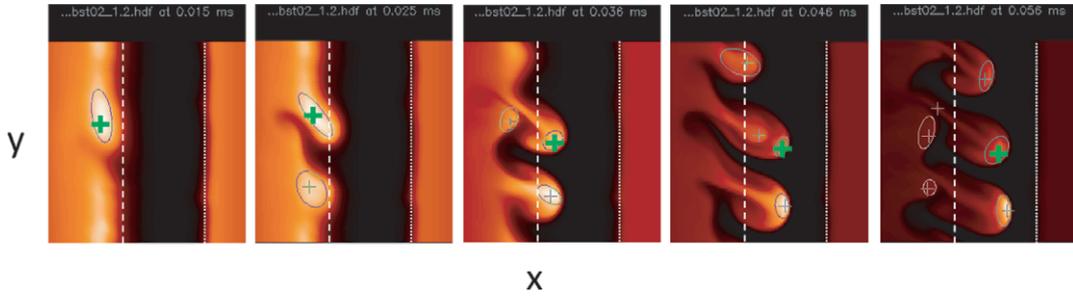

Figure 5. SOLT code simulated normalized GPI image of a seeded blob for the NSTX shot. The vertical coordinate y is binormal (approximately poloidal); x is radial. The time between frames is 10 μs. The core plasma is to the left and the dashed line is the separatrix location; the dotted line is the radial limiter. The green cross marks the seeded blob, which also triggers a secondary blob ejection.

length profile $L_{||}$. Dissipation parameters (plasma viscosity and flow damping) were treated as *ad hoc* input parameters since experimental values were not known. Typical blob spatial sizes, amplitudes and birth locations were extracted from the experimental dataset. A Gaussian blob with the given properties was then superimposed on the background plasma profiles as an initial condition for the SOLT simulation. The blob was tracked until it either disappeared (lost its structure) or travelled radially to a limiter in the far SOL. An example of the resulting synthetic GPI images is shown in figure 5. Note that the background profiles are unstable to curvature-driven instabilities. As a result the emission of a secondary blob is triggered by the seeded blob.

Additionally, simulations were allowed to run to a quasi-steady turbulent state (see sections 4.3 and 4.4). In the self-consistent turbulent state, a balance is maintained between instability of the mean profiles, the turbulent transport induced by the instabilities, and sources. Thus these turbulence simulations required the addition of particle and heat sources to maintain the density and temperature profiles close to experimental values. The electrostatic potential was allowed to evolve freely under the action of Reynolds stress and sheath dynamics, without any additional sources. Thus, radial electric fields and hence $\boldsymbol{E} \times \boldsymbol{B}$ binormal (y-directed) flows were self-consistent with the turbulence.

In each simulation case, as well as in the experiments, it is possible to identify individual blob tracks and fit smoothed trajectories to the positions $x(t)$ and $y(t)$. Differentiating with

respect to time, one obtains

$$\langle a_y \rangle = \left\langle \frac{dv_y}{dt} \right\rangle = \langle \boldsymbol{v} \cdot \nabla v_y \rangle = \frac{\partial}{\partial x} \langle v_x v_y \rangle \quad (1)$$

where the quantities $\langle a_y \rangle$ and $\langle dv_y/dt \rangle$ are computed from averages of 'single-particle' blob trajectories while $\langle \boldsymbol{v} \cdot \nabla v_y \rangle$ and $\partial_x \langle v_x v_y \rangle$ are regarded as statistically averaged fluid quantities in the turbulent steady state.

4.2. Trajectory analysis for seeded blobs

Trajectories for six cases, relevant to the NSTX discharge are shown in figure 6. Figure 6(*a*) is a representative NSTX track obtained by initializing the blob with the mean blob parameters of table 1, and using experimental outer midplane plasma profiles and parameters for other simulation inputs, except that *no mean background flow is imposed*. Thus the v_y of the blob is generated entirely by blob interaction with the plasma and geometry. This track exhibits blob ejection and v_y reversal similar to some of the experimental tracks of figure 2. It is consistent with other experimental data [59] which typically show flows in the electron diamagnetic direction inside the separatrix, reversing to the ion direction in the SOL. The inferred size (amplitude) of the radial and poloidal blob velocities in the edge and SOL are within a factor of two of the experimental values, the directions are the same, and the scale lengths of variation are similar.

Next in SOLT we artificially varied simulation parameters and physics to infer the importance of specific mechanisms
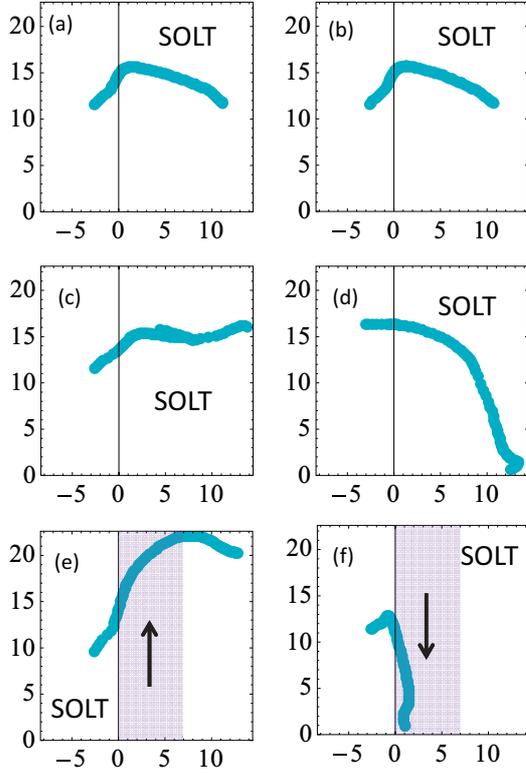
Figure 6. SOLT code seeded blob tracks for the NSTX analysis: (*a*) base, (*b*) fully sheath connected, (*c*) sheath disconnected, (*d*) electron adiabaticity and drifts off, (*e*) imposed SOL $v_{Ey} > 0$, (*e*) imposed SOL $v_{Ey} < 0$. The (horizontal, vertical) coordinates are (x, y) = (radial, binormal).
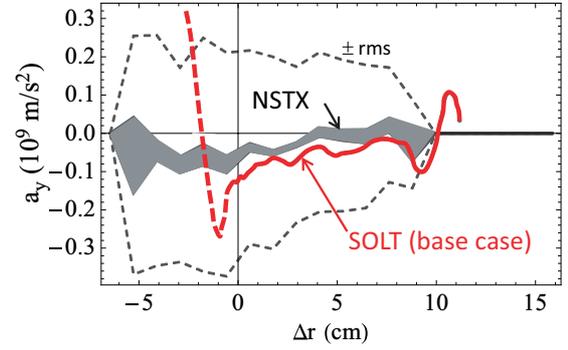

Figure 7. Reynolds acceleration $\langle a_y \rangle$ for seeded blob simulations compared with experimental results for NSTX. The grey curves are experimental data. The central shaded region is the mean acceleration, with statistical uncertainty. The dashed grey lines show the mean $\pm$ rms deviations for the experimental data. The red curve is from the SOLT seeded blob simulation with artificial initial transient shown by the dashed line. A reference acceleration for this case is $a_{y,\text{in}} = 6 \times 10^8 \, \text{m s}^{-2}$. See text for definition.

in the experimental data. Figure 6(*b*) illustrates the track for a completely sheath-connected case (zero collisionality), while figure 6(*c*) is for a completely sheath-disconnected case (large collisionality, no parallel current). We infer that parallel currents in the SOL are important in establishing the blob track and the *y*-acceleration along the track. Figure 6(*d*) shows the result of suppressing electron adiabatic effects (i.e. $\alpha_{\text{dw}} = 0$), and hence the upward electron drift, in the edge region. This blob maintains a stronger dipole charge than the previous case (because adiabatic electrons neutralize the charges by parallel current flow) and is therefore ejected rapidly. It moves downward in the SOL due to the asymmetry of the sheath current–voltage relation, which favours electron loss [56]. (Ion current in the SOL is limited by the ion saturation current.)

Figures 6(*e*) and (*f*) show the result of initializing the simulations with a mean background $\boldsymbol{E} \times \boldsymbol{B}$ flow in the SOL, respectively up in figure 6(*e*) and down in figure 6(*f*). This imposed flow is within the rms range observed in NSTX (see figure 8), but on the high side for purposes of illustration. (Although the background potential evolves freely in the simulations according to equation (A1), during the short duration of these seeded blob simulations, it remains approximately unchanged.) The imposed Gaussian-shaped flow is approximately confined to and centred in the shaded region. This background flow has a shear and vorticity, which induces a bipolar charge layer (through its $\nabla^2 \Phi$) with which the blob charge must interact. For the direction of flow in figure 6(*e*) the charge layer facing the edge region (i.e. near

and just outside the separatrix) is negative. The blob however has acquired a net positive charge through electron adiabaticity [41] in the edge region. (The blob's net positive δn implies a net positive $\delta \Phi$.) Therefore, the blob in 6*e*) is attracted from the edge to the separatrix and experiences an enhanced ejection. This case is that of counter-shear vortex interaction. When the flow is reversed as in figure 6(*f*) the edge blob is repelled from the separatrix and experiences trapping or enhanced confinement. This case is that of co-shear vortex interaction. The sense of the flow shear in figure 6(*f*) is like the mean flow observed in NSTX (see figure 8); this sheared flow acts to enhance edge confinement, and is the blob realization of the well-known mechanism of sheared-flow suppression of turbulence [3, 60]. It is also qualitatively in accord with other NSTX experimental data [61] which showed that blob ejection is suppressed in H-mode, where large sheared flows are present. The size of the flows applied in figures 6(*e*) and (*f*) is comparable to the largest flows seen in the experimental data for this shot.

Note the implications for residual Reynolds stress (i.e. Reynolds stress that is non-zero even when $v_E = 0$): in cases (*a*)–(*d*) the background $\boldsymbol{E} \times \boldsymbol{B}$ flows were suppressed yet Reynolds acceleration, defined in equation (1), still occurs; moreover, response to imposed $\boldsymbol{E} \times \boldsymbol{B}$ flows in (e) and (f) is asymmetric. Thus the charge dynamics of filamentary structures near the separatrix illustrated in the sketches of figure 3 and the simulations of figure 6 constitute significant mechanisms for residual stress.

4.3. Simulation comparisons for NSTX

An experimental database of blobs for the NSTX shot was obtained, consisting of approximately 4000 individual blob images (after filtering for an amplitude threshold of $\delta I/I > 0.6$, blob lifetimes $> 25 \, \mu$s, blob half-max area $> 6 \, \text{cm}^2$). This database resulted in about 400 blob trajectories that could be used in the analysis described by equation (1). In figure 7, results of this experimental database are compared with the base case seeded blob simulation discussed previously. Note
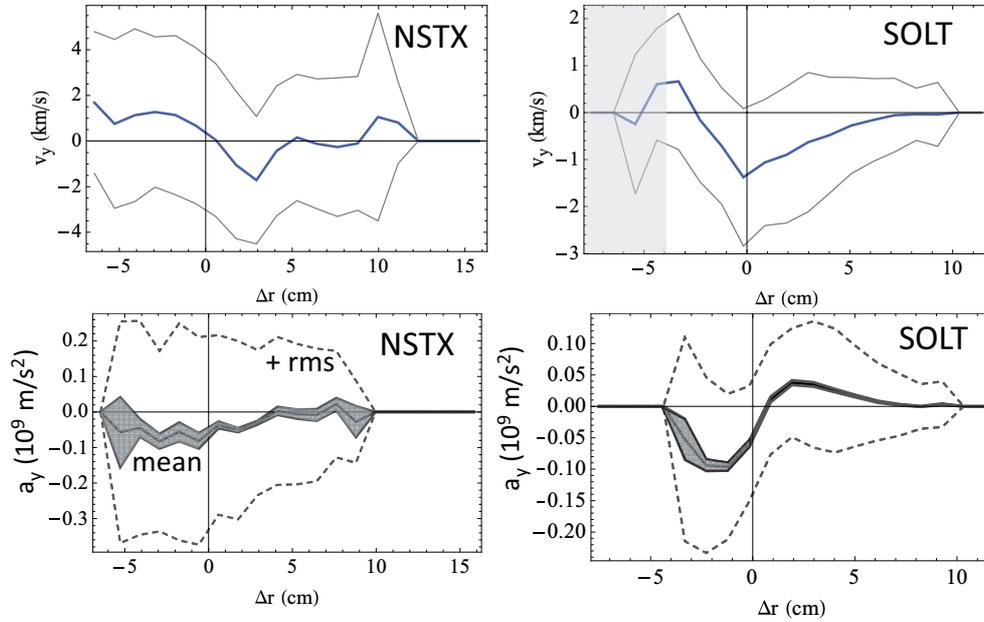
Figure 8. SOLT turbulence simulations (right) compared with NSTX data (left). Top panels are the mean blob v_y (thick blue) $\pm$ rms deviations (thin grey). The shaded region in the upper right SOLT figure may be influenced by the simulation boundary. Bottom panels are mean blob accelerations a_y (grey shading indicates statistical uncertainty) $\pm$ rms deviations (dashed). A reference velocity and acceleration for this case are $v_{in} = 3.6\,\mathrm{km\,s^{-1}}$ and $a_{y,in} = 6 \times 10^8\,\mathrm{m\,s^{-2}}$.

that this base case has no background flow which is again within the rms range observed (see figure 8).

For the NSTX shot, the seeded blob simulation (red curve) does a remarkable job of modelling the experimentally observed mean acceleration, indicated by the thick grey region. (The red dashed portion of the blob simulation is the result of an initial transient as the seeded blob relaxes.) As for figure 6(*a*), this blob was initialized with the mean blob parameters of table 1, and evolved using experimental outer midplane plasma profiles and parameters. The satisfying agreement obtained here is the most direct piece of evidence supporting our claim that the simulated mechanisms, specifically the edge electron diamagnetic velocity profile and changes in edge topology at the separatrix, combined with SOL currents, are *sufficiently* large to explain the Reynolds stress observed in the experiment. That is not to say that they are the *only* mechanisms operative, or that our modelling of these mechanisms is complete. Nevertheless, the point is that starting from a case with no flows, the mechanisms included in the simulations are of sufficient strength to reproduce results similar to the observations. Figure 7 is a key result of our paper.

Note that the typical values of a_y obtained here are of the order of magnitude v^2/l, (where $v \sim 1\,\mathrm{km\,s^{-1}}$ is a typical velocity and $l \sim 1\,\mathrm{cm}$ is a typical scale length for the flows) indicating that the obtained accelerations are indeed significant. This is also evident by the fact the observed trajectories deviate strongly from purely ballistic motion.

A more theory-based normalization from which to assess the scale of a_y (and of v_y in the turbulence simulations to follow) is obtained from the inertial limit for blob convection [6, 7], for which a characteristic velocity is $v_{in} = c_s(\delta_b/R)^{1/2}$ where δ_b is blob radius given in table 1. The quantity v_{in} is the maximum convection velocity achieved by blobs that are

not significantly slowed by sheath or other dissipative effects; in practice blobs are usually slower. From this, we form a characteristic acceleration $a_{y,in} = v_{in}^2/\delta_b$. (Although v_{in} really represents a velocity in the x-direction, for significant effects on the trajectory, changes in v_y must be comparable to v_x so it is suitable for present purposes.) For the NSTX case we find $v_{in} = 3.6\,\mathrm{km\,s^{-1}}$ and $a_{y,in} = 6 \times 10^8\,\mathrm{m\,s^{-2}}$ which is comparable in order of magnitude to both observations and simulations.

The experimentally observed rms deviations in figure 7 are large compared to the mean. This indicates the presence of oscillating zonal flows, which can be considered as resulting from blob-blob interactions. Furthermore, the calculated accelerations depend on the instantaneous background flows. Quasi-steady turbulence simulations (rather than the more straightforward seeded blob simulations) are required to further elucidate this. The SOLT turbulence simulations are compared with experimental results in figure 8.

Although the SOLT simulations for the NSTX case capture some qualitative aspects of the data and give similar results (factor-of-two level agreement) for radial scales lengths, velocities and accelerations, some detailed differences are apparent in figure 8. In the SOLT simulation the minimum blob velocity v_y occurs on the separatrix while in the NSTX experiment it is shifted further out. The SOLT simulation of a_y also shows a positive peak in the SOL which is not seen in the NSTX data. This positive peak in a_y can be traced to the mean sheared $\boldsymbol{E} \times \boldsymbol{B}$ flow in the simulation which has a strong local minimum of $-0.6\,\mathrm{km\,s^{-1}}$ at $\Delta r = 1\,\mathrm{cm}$. Although flow reversal near the separatrix is commonly observed in NSTX and other experiments, it is usually a stronger effect in SOLT modelling, probably because of deficiencies in the description of geometry, divertor sheath boundary conditions and SOL dissipation in general.
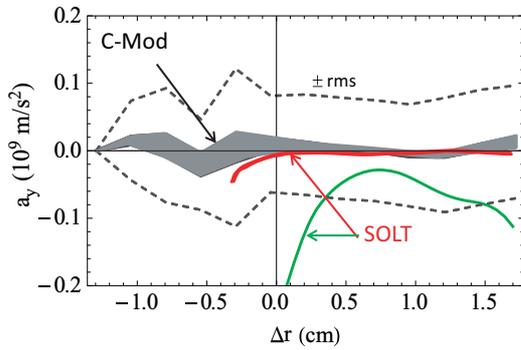
Figure 9. Reynolds acceleration $\langle a_y \rangle$ for seeded blob simulations compared with experimental results for Alcator C-Mod. The grey curves are experimental data. The central shaded region is the mean acceleration, with statistical uncertainty. The dashed grey lines show the mean $\pm$ rms deviations for the experimental data. The curves are from the SOLT seeded blob simulations showing the midplane test case (green), and the disconnected case with extra friction (red). A reference acceleration for this case is $a_{y,\text{in}} = 2.6 \times 10^9 \,\text{m s}^{-2}$.

The agreement in a_y of simulation with experiment is less precise than for the seeded blobs for two main reasons. Firstly, the turbulent system is not guaranteed to maintain the reference profiles to a high degree of accuracy. Secondly, the statistics of the blobs generated in the turbulence simulations is similar, but not identical, to those observed in the experiment. The turbulent simulations obviously provide a more self-consistent description and capture large rms fluctuations of v_y and a_y relative to their means.

4.4. Simulation comparisons for Alcator C-Mod

The NSTX case was a low collisionality case; now for contrast we consider a high collisionality case in Alcator C-Mod. Previous theoretical and experimental work on blobs has shown that edge turbulence and blob speed depends on collisionality [6, 7]. An analysis of the blob accelerations for this C-Mod shot were carried out as previously described. The experimental database consisted of approximately 6000 individual blob images (after filtering for an amplitude threshold of $\delta I/I > 0.2$, blob lifetimes $>25 \,\mu$s, blob half-max area $>0.2 \,\text{cm}^2$) and resulted in about 600 blob trajectories, which were employed to obtain figure 9.

For this highly collisional C-Mod case, SOLT simulations are more challenging because collisionality is expected to allow the blob-filaments to acquire structure (e.g. temperature gradients) along the magnetic field line. These gradients are allowed in the high collisionality (conduction limited) regime, but difficult to model in the 2D SOLT code.

When seeded blob simulations were carried out for the C-Mod case using midplane values, and no flow damping, significant a_y resulted, as shown by the green curve in figure 9. The C-Mod experimental result of near-zero mean a_y could be modelled satisfactorily only by making several additional assumptions (red curve): complete parallel sheath disconnection in the SOL, partial collisional disconnection in the edge, and finite flow damping, $\nu/\Omega_i = 0.02$. Theoretically, in our model, flow damping is equivalent to friction and also to extra charge dissipation by cross-field currents [6, 7]. The latter are expected when X-points (and their associated

thin radial fans [62, 63]) are present downstream along B. Friction could also be provided in this shot by neutral collisions [64]. Previous modelling of the effect of neutral density on turbulence damping suggest the plausibility of this mechanism [65]. With these simulation parameter choices, an acceleration is obtained that is close to the experimentally observed band.

While these parameter choices can be viewed simply as empirical fits, they can also be motivated by considerations of the collisionality regime (as indicated in table 1) and geometrical effects. The C-Mod collisionality parameter Λ exceeds unity. This means [6, 7] that Coulomb collisional resistivity is more important than sheath resistivity in impeding parallel current flow. The SOLT model only describes dynamics in the two directions perpendicular to B. Parallel physics is described by analytical closure relations. Although the collisional closures employed in SOLT do permit parallel sheath disconnection in the SOL at large values of Λ (see appendix A), the model is not expected to be accurate quantitatively. In the collisional regime T_e decreases from its midplane value along the field line as the divertor is approached, possibly resulting in larger effective values of Λ than those estimated from midplane parameters. Since these 3D effects cannot be modelled quantitatively, we choose to just take the extreme limit of complete disconnection in the SOL ($\Lambda \to \infty$) as an interesting limiting case.

When parallel currents are impeded by collisions, blob polarization charges are instead neutralized by current paths that flow in the perpendicular direction. These cross-field currents (ion polarization currents) flow most easily in the X-point region because thin radial fans develop there due to strong local magnetic shear. Enhanced ion polarization currents increase the effective inertia of the blob, and slow it down [66], effectively providing an extra friction. Because the cross-field X-point current is also a 3D effect, it is difficult to model quantitatively in SOLT. The chosen value for the flow damping parameter was determined empirically. As observed in previous work dedicated to the study of this effect [66] it can result in order unity modifications to the dynamics. (See the η-high Geometry-on and Geometry-off cases in that reference.)

Because of these semi-empirical parameter choices, quantitative conclusions cannot be reached for this high collisionality case. Rather it is concluded that important additions to the physics, not present in our analysis, are needed for quantitative modelling.

Given these caveats, SOLT turbulence simulations for these parameter choices are shown in figure 10. These simulations confirm the seeded blob results and qualitatively reproduce the experimental data: small mean flows and accelerations with significant rms fluctuations due to the turbulence. For the C-Mod case the characteristic velocity and acceleration are $v_{\text{in}} = 3.2 \,\text{km s}^{-1}$ and $a_{y,\text{in}} = 2.6 \times 10^9 \,\text{m s}^{-2}$. These values, especially $a_{y,\text{in}}$, are significantly larger than the values shown in figure 10, which is again indicative, at a more heuristic level, of the likelihood of strong dissipative mechanisms at work.

4.5. Elliptical blob tilting and the Reynolds stress proxy

So far the Reynolds stress analysis in these discharges has relied on blob trajectories, but we also have information
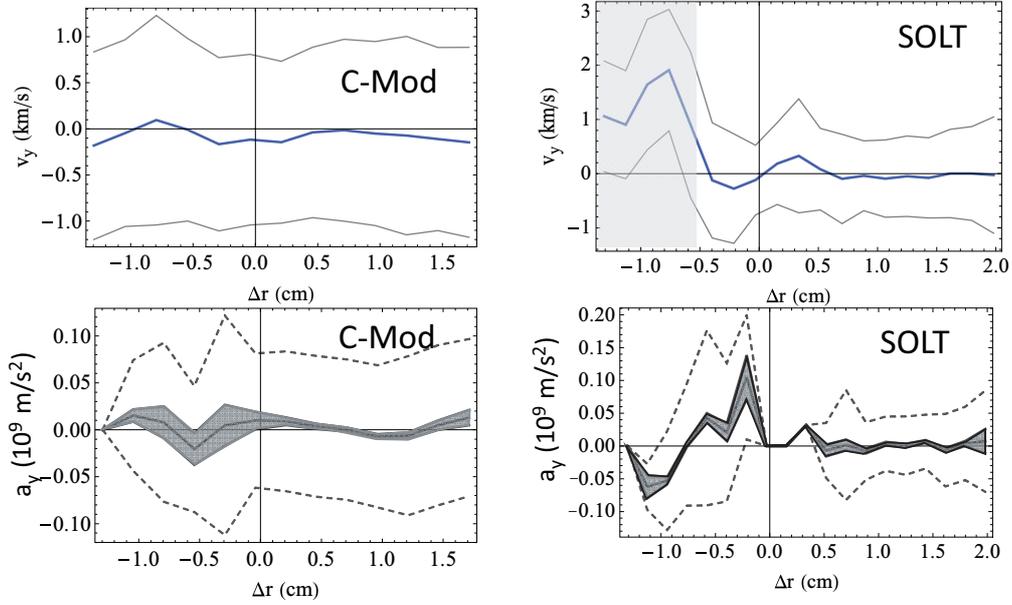
Figure 10. SOLT turbulence simulations (right) compared with Alcator C-Mod data (left). See figure 8 for a description of the curves. A reference velocity and acceleration for this case are $v_{in} = 3.2\,\mathrm{km\,s^{-1}}$ and $a_{y,in} = 2.6 \times 10^9\,\mathrm{m\,s^{-2}}$.

about the elliptical deformation of the structures. To analyse these deformations, we assume that the ellipticity and tilt angle of the blob electrostatic potential are similar to those of the density and temperature, and hence the GPI emission, notwithstanding possible detailed differences in internal structure. The similarity is most easily justified in the sheath-connected regime where analytical solutions are available in some limits, and intuition is simplest. In the general case, however, assuming a reasonably coherent and long lived propagating structure, we can still argue that the density inside the structure convects along streamlines which are also equipotential surfaces. So the assumption that the ellipticity and tilt of the density or GPI intensity structure is similar to that of the potential seems reasonable.

Given this assumption, it is shown in appendix B that a normalized proxy for the Reynolds stress, hereafter referred to as the RSP, is given by

$$\mathrm{RSP} = -\sin(2\theta)[1 - (r_2/r_1)^2] \qquad (2)$$

where θ is the tilt angle (measured clockwise from the positive ΔR or x axis) and r_2 (r_1) is the major (minor) axis of the best-fit ellipse. In the absence of either ellipticity or tilt, there is no Reynolds stress. See figures 11(*a*) and (*b*).

Figures 11(*c*) and (*e*) show the results of an RSP analysis for the NSTX and Alcator C-Mod shots using experimental data. Each dot in these figures represents the shape and orientation versus location of a blob at a particular time. Results are qualitatively the same for different blob selection criteria. Figures 11(*d*) and (*f*) show the RSP analyses from the corresponding SOLT turbulence simulations for NSTX and C-Mod. Qualitative features of the experiment are reproduced, namely radially varying structure of the RSP in the NSTX shot, and little in the C-Mod shot. An experimental measurement of the Reynolds stress was not available for this data (hence the motivation for defining a proxy); however, it is interesting to compare the qualitative features of the mean RSP with the mean

Reynolds stress calculated in the simulation. The latter result will be shown in figure 13. The mean flow $\langle v_y \rangle$ is driven in the direction of $-\partial_x \langle \mathrm{RSP} \rangle$. Qualitatively, it can be seen that the mean flow in figure 8 corresponds to the RSP gradient for the NSTX case. In the C-Mod case, there is insufficient variation of the RSP with radius to make differentiation meaningful, but in this case the mean a_y is too small to drive significant means flows, consistent with the analysis in figure 9 and with the small flows observed in figure 10. A different analysis method of zonal flows for this (and other) Alcator C-Mod shots was described in [67]. Small mean zonal flows were also reported for this C-Mod shot (1100824017), and the oscillating zonal flows were found to have a broadband frequency spectrum.

It is significant that for both the NSTX and C-Mod shots, an order unity variation of the RSP (essentially from -1 to 1, i.e. over the full possible range) is observed. This shows that significant instantaneous shearing stresses are acting on the blobs regardless of whether there are mean flows or not. In previous theoretical and simulation work [43] we showed that order unity shearing deformations of the blob structure are consistent with the idea that shearing affects the blob dynamics. The dimensionless shearing parameter $v_y' \tau$ provides a simple estimate of when local $\boldsymbol{E} \times \boldsymbol{B}$ shear significantly affects blob tilt and ellipticity. Here τ is the blob convection-transit time $\tau \sim \delta_b / v_{x,b}$ (comparable to the inverse auto-correlation time, or typical inverse linear growth rate) and $v_y' \sim v_y / L_x$. For example, for the NSTX case, an analysis of the blob tracking database yields the mean flow estimates $v_y \sim 1\,\mathrm{km\,s^{-1}}$, $L_x \sim 2\,\mathrm{cm}$, $v_{x,b} \sim 0.5\,\mathrm{km\,s^{-1}}$, $\delta_b \sim 2\,\mathrm{cm}$ and results in $v_y' \tau \sim 2$ which implies significant $\boldsymbol{E} \times \boldsymbol{B}$ shearing from mean flows. This is consistent with significant shearing effects as deduced from figure 11. When the shearing rate is of this magnitude or larger, it both creates isolated blob structures from radial streamers [43, 46, 68] and begins to suppress turbulent radial transport, e.g. consistent with the discussion of figure 6(*f*).

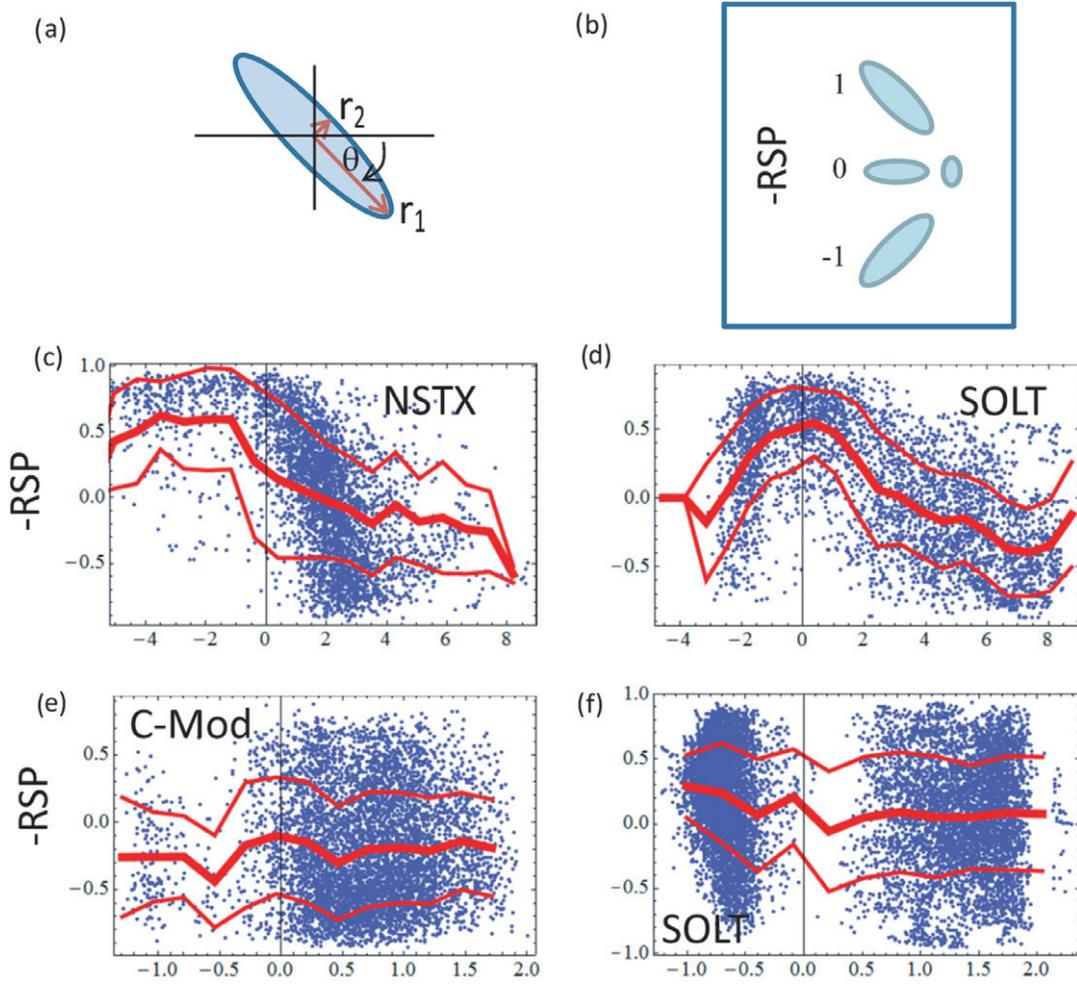As an aside to the main point, note that there is a prominent gap in Δr in the SOLT simulation of figure 11(*f*). The gap

9

Figure 11. RSP definition and simulation–experiment comparisons: (*a*) sketch of tilted elliptical blob and (r_1, r_2, θ) used in defining the RSP; (*b*) sketch of blob shapes and orientations and the corresponding values of RSP; (*c*) RSP for NSTX experimental data and (*d*) for SOLT simulation; (*e*), (*f*) C-Mod experimental data and corresponding SOLT simulation. The lines overlaying the RSP dots indicate mean (thick) ±standard deviation (thin) values of the RSP versus position.

contains no blobs meeting the detection criteria. (See also a_y in the SOLT result of figure 10.) This gap is the result of the GPI helium line emission function which maximizes at the centre of the gap for the background density and temperature profiles of this shot. When near such a maximum, the GPI emission is insensitive to any perturbation caused by the blob. Note that a similar, but less dramatic, gap is also present at a smaller radius in the experimental results of figure 11(*e*). The SOLT synthetic GPI diagnostic uses an approximate single state collisional radiative model [69–71], which may bear on the discrepant gap location.

The presence of time-dependent flows as well as mean flows in these simulations is suggested by the large rms deviations apparent in figures 8 and 10, as well as by the large spread in RSP in figure 11. The time-dependent flows are further illustrated by the single-point frequency spectrum of v_{Ey} shown in figure 12 for NSTX. (Spectra for the C-Mod case are qualitatively similar.) Here v_{Ey} is the y (i.e. binormal) component of the $E \times B$ velocity taken from the simulation. It is not to be confused with the y-velocity of the blobs as determined by blob tracking used elsewhere in the paper. For this analysis (taken at a single point in the x, y plane) no poloidal averaging and no time averaging or smoothing

has been done. The spectrum is shown at the separatrix location, where from figure 8 (upper right) we see that the mean flow and the rms deviation are almost equal. This spectrum in figure 12, which is typical of both density and velocity fluctuations in the present simulations, is also qualitatively similar to experimental data (see e.g. figure 9 of reference [10]). Note the approximate power law dependence in each of two separate bands, here 2–30 kHz and $f > 30$ kHz. The 30 kHz breakpoint corresponds roughly to the inverse auto-correlation time (self-transit time) of a blob ($v_b/\delta_b \sim 1/\tau_c$) while the 2 kHz rate is a typical rate at which the source functions refuel the core region after a blob loss event. The inset plot is on a linear scale and emphasizes low frequency ($f < 5$ kHz) oscillations that are sometimes seen and related to zonal flows. Figure 12 clearly indicates that low frequency flows exist in addition to the zero frequency (mean) flows. Theoretical work [3, 12, 72] suggests that both types of flows are of interest for interaction with turbulence, and may even be competitive [72].

4.6. Turbulent flow generation and net force

Encouraged by the qualitative agreement of SOLT turbulence simulations with the experimental results shown in
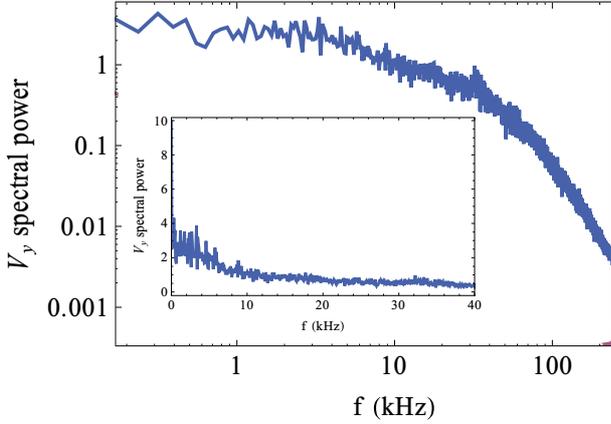
Figure 12. Single-point frequency spectrum of the $E \times B$ drift v_{Ey} taken at the separatrix from SOLT code simulations of the NSTX shot. The inset shows the 0–40 kHz spectrum on a linear scale.

figures 7–11, we can employ the simulations to calculate quantities not directly available from the data. One such quantity that is frequently of interest [73] is the turbulence production rate

$$P_t = -\langle v_x v_y \rangle \frac{\partial \langle v_y \rangle}{\partial x} \quad (3)$$

where the zonal averages $\langle \ldots \rangle$ are taken over the y-coordinate at each time point, and the entire expression is then time-averaged to obtain a mean and its corresponding rms fluctuations. The turbulence production rate and more generally the energetics of turbulence has been studied in [4, 5] including the transfers between zonal flows, electrostatic fluctuation energy, magnetic fluctuation energy, and density sidebands associated with geodesic acoustic modes. The latter two effects are outside the scope of the present 2D electrostatic model.

The result of evaluating equation (3) for the NSTX simulation, shown in figure 13, indicates $P_t < 0$, i.e. energy is being transferred from the turbulence to the mean flows as expected. P_t has dimensions of v^2/τ. Taking a typical velocity as $1 \, \mathrm{km \, s^{-1}}$ (see e.g. figure 8) and a typical blob time-scale as $\tau_c \sim 30 \, \mu s$, a characteristic order of magnitude is $v^2/\tau_c \sim 0.3 \times 10^{15} \, \mathrm{cm^2 \, s^{-3}}$. Consequently, the observed $P_t \sim 10^{15} \, \mathrm{cm^2 \, s^{-3}}$ is significant. Free energy in the pressure gradient generates turbulent energy which is then partially transferred to mean flows.

Results for P_t in the high collisionality C-Mod shot (not shown) are qualitatively similar in shape, but the order of magnitude is much smaller $\sim 10^{12} \, \mathrm{cm^2 \, s^{-3}}$ indicating a negligible transfer of energy to mean flows for this shot; this is consistent with the much smaller mean flows that are observed.

Of course the turbulence, which manifests itself in the outwardly ejected blobs (figure 2), implies particle, momentum, and heat fluxes across the separatrix. The transport of momentum across the separatrix results in a net force on the plasma. The strength of this force per unit of power flowing across the separatrix is given by the ratio of momentum to heat flux:

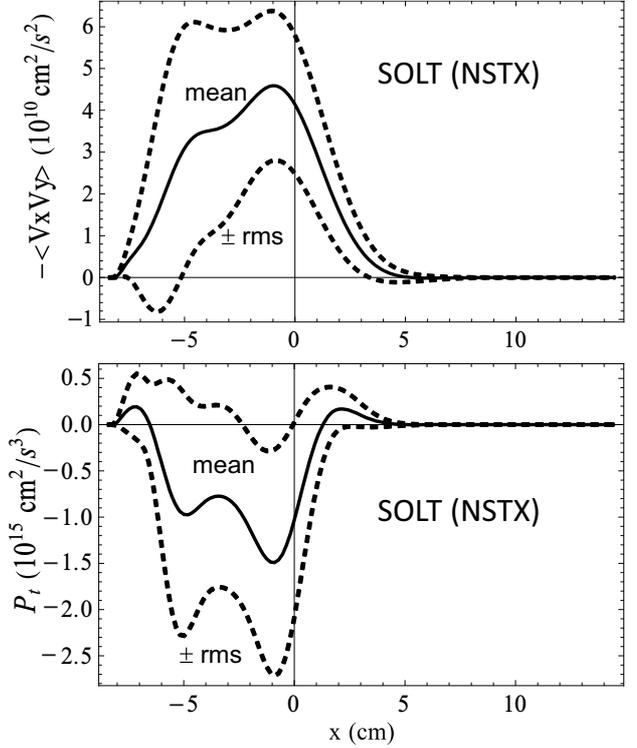$$\frac{F_\perp}{P} = \frac{\langle n v_x v_y \rangle}{\langle 2nT v_x \rangle} \quad (4)$$

Figure 13. Negative of the Reynolds stress (upper panel) and turbulence production rate P_t (lower panel) from the SOLT simulation of the NSTX shot showing the mean value (solid) and mean $\pm$ rms deviations (dashed). $P_t < 0$ implies turbulent energy is being transferred to mean flows.

where here $P = P_{\mathrm{sep}}$ is power (not to be confused with P_t), and in the expression for the heat flux, the factor of 2 accounts for the ion contribution assuming $T_e = T_i$. From the simulations, we estimate the perpendicular force on the plasma as $F_\perp/P = 0.8 \, \mathrm{N \, MW^{-1}}$ for the NSTX shot, and $F_\perp/P < 0.05 \, \mathrm{N \, MW^{-1}}$ for the C-Mod shot.

The net force on the plasma is closely related to the fact that the SOL is a loss channel for momentum [74]. The momentum flux $\langle n v_x v_y \rangle$ appears under a radial derivative in the zonal momentum equation (see appendix A),

$$\frac{\partial}{\partial t} \langle n v_y \rangle + \frac{\partial}{\partial x} \langle n v_x v_y \rangle = \int_0^x \mathrm{d}x \, \alpha_{\mathrm{sh}} \langle J_{||} \rangle + \mu \frac{\partial^2}{\partial x^2} \langle v_y \rangle \quad (5)$$

hence on closed surfaces, absent momentum losses, localized turbulence with its Reynolds stress can redistribute momentum radially, driving bipolar flows, but it cannot drive a net radially averaged flow. However, when a radial zone (the SOL) permits momentum loss (the α_{sh} term), net forces and flows on the core plasma can result. This mechanism has previously been cited as a way in which blob ejection could drive intrinsic flows [74, 75].

When projected onto the toroidal direction, $F_\perp$ contributes to the so-called intrinsic torque driving toroidal rotation. In order of magnitude the $1 \, \mathrm{N \, MW^{-1}}$ level is similar to values obtained near the separatrix on DIII-D [76]. Because of the simplified non-toroidal geometry of the SOLT model, we cannot claim that this effect explains intrinsic toroidal rotation, but it would appear to represent a competitive effect that cannot be ignored. Furthermore, the torque exists in the absence of

background E_r driven flows as illustrated in figures 6(*a*)–6(*d*), and therefore qualifies as a symmetry-breaking or residual Reynolds stress.

5. Discussion and conclusions

A combination of experimental data analysis, seeded blob simulations, and turbulence simulations have been employed to study the interaction of blob-filaments with sheared flows. Here we consider a rather general definition of blob-filaments that includes both isolated wave crests in the edge region, and structures that have been ejected into the SOL. Theoretical mechanisms related to radial inhomogeneity, and parallel sheath currents from radial changes in magnetic topology cause the generation of Reynolds stress, including a so-called residual Reynolds stress that is non-zero even when there are no background $E \times B$ flows. An important conclusion, illustrated in figures 7 and 8, is that these mechanisms are sufficiently strong to explain the observed Reynolds acceleration and hence the generation of blob perpendicular (approximately poloidal) flows (their size, radial scale, direction and reversal across the separatrix) in a low collisionality NSTX shot. We cannot rule out the possibility that additional mechanisms, not included in our model, are also important. A selected high collisionality Alcator C-Mod shot shows very small mean sheared flows. It was found (see figure 9) that many characteristics of this shot could be simulated by additionally assuming (i) collisional disconnection of the midplane from the divertor sheaths (e.g. due to a low divertor temperature), and (ii) flow damping or equivalently charge dissipation by radial currents, possibly due to X-point effects. This portion of the study pointed to additional 3D physics not included here but needed for quantitative modelling of high collisionality cases. In both the NSTX and C-Mod cases mean and oscillating zonally averaged flows are sufficiently strong to affect blob dynamics and transport, as shown by the blob trajectories and resulting accelerations (figures 7 and 9) and the elliptical deformation of the blob structures (figure 11).

In addition to 3D effects, it is possible that some of the conclusions of the present paper could be modified by electromagnetic effects which are not considered here. Some specific electromagnetic effects on blob-filaments have been discussed in review articles [6, 7] and in [77]. These particular effects are not expected to *qualitatively* affect the conclusions of the present study. For a more general discussion of electromagnetic effects on edge turbulence the reader is referred to [4, 5]. Numerical SOL modelling of blob-filaments which incorporates electromagnetic effects remains as a topic of future investigations.

The studies described here have implications for SOL interactions of blobs with plasma-facing components. As evidenced by figures 6(*e*) and 6(*f*), blob trajectories, and their radial (*x*) penetration into the SOL are influenced by their motion in the binormal (*y*) direction, and in particular by the flow shear in the near-separatrix region. The near-SOL heat flux width may be set by the radial penetration of blob-filaments into the SOL, arising from a competition between the radial blob velocity and the parallel expansion velocity of heat towards the divertor plates. Judiciously driven sheared flows in the SOL could increase the SOL width, likely at the expense of edge confinement, such as the 'reverse' flows shown in figure 6(*e*) which enhance the blob ejection velocity due to polarization charge interactions. These flows could be produced by toroidally symmetric biasing, in contrast to the toroidally dependent biasing studied elsewhere [78–80].

There are also implications for understanding L–H transition physics. Recent work has advanced the hypothesis that mean and oscillating zonal flows build up in the L-mode phase as additional heating power is applied, until eventually transport suppression triggers profile steepening, and an H-mode phase in which sheared $E \times B$ flows are maintained by the role of the large ion pressure gradient in radial force balance. The present studies add to this picture by showing how seed flows are initially established in ohmic plasmas.

While our work has concentrated on perpendicular forces and flows, there are clearly implications for toroidal torques and flows near the separatrix and in the SOL. Because our model does not contain all relevant toroidal effects, we can only say the toroidal projection of the perpendicular dynamics discussed here is likely to be a significant contributor in the toroidal direction. Recent work [37] has identified a theoretical mechanism relevant to toroidal flows which changes sign when the X-point topology is changed relative to the grad-*B* drift direction. On the other hand, the residual stress mechanism discussed here in connection with figure 6, and responsible for the forces producing figure 13, may play a role in setting up a component of toroidal plasma rotation which does not change when X-point topology is changed. Both types of flows have been observed [81]; the latter is essentially a toroidal rotation of the SOL in the co-current direction that is strong at low densities and weaker at high densities.

Aside from these more speculative implications, the main results of our paper are to be found in figures 3, 6 and 7 which illustrate the mechanisms responsible for flow generation by blob-filament dynamics in the near-separatrix region and the simulated comparisons of those mechanisms with experimental data. While the simulation model employed here has many caveats, such as cold ions, electrostatics, model 2D geometry, fluid theory, and the use of a simplified drift-wave physics model, it does capture the essence of nonlinear polarization and $E \times B$ dynamics in the separatrix region, and those essentials would appear to be sufficient as a framework for understanding many aspects of the experimental data.

Acknowledgments

Appendix A. The SOLT model

Computations are carried out with the 2D Scrape-Off-Layer Turbulence (SOLT) code [43]. Analytical closure relations are employed to describe the parallel dynamics. For example, the relationship of parallel current $J_{||}$ to Φ is prescribed by a sheath closure on open field lines (generalized to allow for collision-dominated regimes), and a Wakatani–Hasegawa-like model [82] for $J_{||}$ is employed on closed field lines to capture basic drift-wave physics.

The fundamental equations for the SOLT model are the vorticity, continuity and energy conservation (or alternatively temperature) equations

$$\frac{\mathrm{d}}{\mathrm{d}t} \nabla \cdot n \nabla \Phi = A_{\mathrm{dw}}(\Phi, n) + \alpha_{\mathrm{sh}} J_{||} - \beta \frac{\partial (nT)}{\partial y} \quad \text{(A1)}$$

$$\frac{\mathrm{d}n}{\mathrm{d}t} = A_{\mathrm{dw}}(\Phi, n) - \alpha_{\mathrm{sh}} \left(n T^{1/2} - J_{||} \right) \quad \text{(A2)}$$

$$\frac{\mathrm{d}T}{\mathrm{d}t} = -\alpha_{\mathrm{sh}} \frac{q_{||}}{n}. \quad \text{(A3)}$$

Here we employ dimensionless notation (using the Bohm normalization with time-scale $\Omega_{\mathrm{ci}} = ZeB/m_{\mathrm{i}}c$ and space scale $\rho_{\mathrm{sr}} = c_{\mathrm{sr}}/\Omega_{\mathrm{ci}}$ where $c_{\mathrm{sr}}^2 = T_{\mathrm{er}}/m_{\mathrm{i}}$ and T_{er} is a reference temperature for the normalization). The simulation plane is denoted as the (x, y) plane where x is the radial direction and y is binormal (approximately poloidal). The convective derivative is written as $\mathrm{d}/\mathrm{d}t = \partial/\partial t + v \cdot \nabla$ where $v = e_z \times \nabla \Phi$. A_{dw} is the drift-wave operator

$$A_{\mathrm{dw}}(\Phi, n) = \alpha_{\mathrm{dw}} \bar{T}^{3/2} \{\Phi - T \ln n\} \quad \text{(A4)}$$

$$\alpha_{\mathrm{dw}} = \frac{2k_{||}^2 v_{\mathrm{te}}^2}{\nu_{\mathrm{ei}} \Omega_{\mathrm{i}}} \quad \text{(A5)}$$

where for any quantity Q, $\langle Q \rangle \equiv \bar{Q}$ denotes the zonal or y average-part and $\tilde{Q} \equiv \{Q\} \equiv Q - \bar{Q}$ denotes the fluctuating part. Thus A_{dw} enforces a Boltzmann response on fluctuations when the coefficient α_{dw} is large, in the spirit of the Wakatani–Hasegawa adiabaticity parameter. Note that the flux-surface or y-average of A_{dw} vanishes (as it must since it arises from $\nabla_{||} J_{||}$ on closed surfaces).

Other coefficients appearing in the model are: the sheath conductivity parameter

$$\alpha_{\mathrm{sh}} = \frac{\rho_{\mathrm{sr}}}{L_{||}} \quad \text{(A6)}$$

where $L_{||}$ is the midplane-to-divertor-plate connection length in the SOL and ρ_{sr} is the reference sound gyro-radius, and the curvature drive parameter

$$\beta = \frac{2\rho_{\mathrm{sr}}}{R} \quad \text{(A7)}$$

where R is the effective radius of curvature (approximately the major radius of the torus). In this paper $L_{||}$ is estimated from field line tracing using experimental equilibrium flux surface reconstruction data. A logarithmic fit [49] near the separatrix is employed.

To close the system of equations, the parallel current and heat flux $J_{||}$, $q_{||}$ must be expressed in terms of the dynamic variables Φ, n and T. A set of closure relations, valid for a range of collisionality regimes from conduction limited to sheath-connected, is employed here. In the sheath-connected limit the parallel current and heat flux are given by

$$J_{||\mathrm{SL}} = n T^{1/2} \left(1 - \mathrm{e}^{(\Phi_B - \Phi)/T} \right) \quad \text{(A8)}$$

$$q_{||\mathrm{SL}} = s_E n T^{3/2} \mathrm{e}^{(\Phi_B - \Phi)/T} \quad \text{(A9)}$$

where $\Phi_B \sim 3\,\mathrm{T}$ at the sheath, and $s_E \sim 6$ is the sheath energy transmission factor. In the simulations of this paper we take $\Phi_B = 0$, which corresponds to a cold divertor plate temperature relative to the midplane temperature. In the collisional (conduction limited) case we employ

$$J_{||\mathrm{CL}} = \frac{1.96 n T^{1/2}}{\Lambda} \frac{(\Phi_B - \Phi)}{T} \quad \text{(A10)}$$

$$q_{||\mathrm{CL}} = \frac{3.2 n T^{3/2}}{\Lambda} \quad \text{(A11)}$$

where the collisionality parameter Λ is given by

$$\Lambda = \frac{\nu_{\mathrm{ei}} L_{||}}{\Omega_{\mathrm{e}} \rho_{\mathrm{s}}} \quad \text{(A12)}$$

Λ is related to the SOL electron collisionality parameter $\nu_{*\mathrm{e}} = L_{||}/\lambda_{\mathrm{ei}} = \Lambda (m_{\mathrm{i}}/m_{\mathrm{e}})^{1/2}$, where λ_{ei} is the electron mean free path for collisions with ions. These parallel closures are Padé-interpolated to provide a smooth connection between the sheath and conduction limited cases. Flux limits are also imposed. See [49] for a discussion of additional details.

The SOLT code solves the vorticity equation, by splitting equation (A1) into zonally averaged and fluctuating parts. The vorticity advection term in the zonally averaged part is manipulated into a conservative form which competes with a sheath sink term in the SOL, and also with explicit *ad hoc* dissipation due to viscosity and (if non-zero) friction. No prescribed momentum sources are employed. (See equation (5) of the main text.) The Boussinesq approximation is employed on the fluctuating part. Small diffusive terms (respectively $\mu \nabla^4 \Phi$, $D_n \nabla^2 n$, $D_T \nabla^2 T$) are usually added to the right-hand sides of equations (A1)–(A3) to absorb high-wavenumber fluctuations before they cascade to the scale of the numerical grid. A friction term $(-\nu \nabla^2 \Phi)$ can also be added to the vorticity equation to model Alfvén wave emission, neutral collisions and other frictional dissipative effects. Further discussion of the SOLT model is given in previous publications [43].

Finally, particle and heat sources are added to the density and temperature equations for the turbulence simulations, in order to allow a quasi-steady state to be maintained in the presence of SOL losses. For the analysis of experimental shots, the sources are implemented by relaxing the turbulent n and T profiles to reference target profiles obtained from the experiment, such as those shown in figure 4. Following earlier work [43], this is achieved by invoking 'spring-loaded' sources: the density and temperature profiles relax to the target values with a specified time constant. The *ad hoc* source relaxation rate is chosen to be of order c_{s}/R in the edge, and is taken smoothly to zero in the SOL so that the SOL profile evolution is determined by turbulent transport and parallel losses. The potential profile is not forced, but evolves (without additional source terms) according to equation (A1). Vorticity

and potential start from a zero-value initial condition except for the seeded blob simulations discussed in figures 6(*e*) and (*f*). In this case an initial background flow velocity was imposed and was approximately invariant throughout the short duration of these simulations.

The simulations in this paper employed the following dimensionless parameters: for the NSTX base case seeded blob simulations $\beta = 0.0060$, $D_n = D_T = 0$, $\mu = 0.2$, $\nu = 0$, $\alpha_{\mathrm{dw0}} = 0.083$, $Z_{\mathrm{eff}} = 2$, and $\alpha_{\mathrm{sh5}} = 0.00105$ (i.e. the value at $x = 5$ cm, see figure 4 for profiles); for the NSTX turbulence simulations, parameters were the same except that $D_n = D_T = 0.001$, a smaller value of $\mu = 0.05$ was employed to permit sustained turbulence, and the effective connection length was arbitrarily reduced by a factor of 2 to give $\alpha_{\mathrm{sh5}} = 0.00052$ to prevent an excessive (and experimentally unobserved) buildup of density in the SOL. For the C-Mod base case seeded blob simulations (midplane parameters yielding the green curve in figure 9) $\beta = 0.00089$, $D_n = D_T = 0$, $\mu = 0.2$, $\nu = 0$, $\alpha_{\mathrm{dw0}} = 0.0076$, $Z_{\mathrm{eff}} = 2$ and $\alpha_{\mathrm{sh1}} = 6.5 \times 10^{-5}$; the disconnected frictional case (red curve in figure 9) modified the parameters to $Z_{\mathrm{eff}} = \infty$, $\alpha_{\mathrm{dw0}} = 0.0019$, $\nu = 0.02$; and the turbulence simulations employed the later parameter set with in addition $D_n = D_T = 0.001$. In the present paper, simulations are initialized with the reference density and temperature profiles, plus a single seeded blob. Due to the instability of the profiles, a quasi-stationary turbulent state ultimately develops.

The numerical value of viscosity μ used in these simulations was chosen to be relatively large (much larger than would be expected theoretically from gyro-viscosity in the Braginskii model) to increase the coherency of the blob structures [83]. This makes the task of blob tracking more robust and also results in blob images that more closely resemble the experimental camera images. Since the value of μ is *ad hoc*, it is important to assess the sensitivity of results to changes in μ. Tracks of the centroids for seeded blobs and time histories of their velocities and accelerations show changes of only a few per cent, to at most 10 per cent, when μ is reduced from the default value of 0.2 to $\mu = 0.1$. At excessively large values of μ, on the order of 1, the changes become quite significant. On the other hand, the friction coefficient ν has a direct effect on the blob velocity and acceleration, as illustrated in the C-Mod study, figure 9. When ν exceeds $\mathrm{d}/\mathrm{d}t$ from the inertial term in the vorticity equation (which is roughly of order v_b/δ_b), the blob velocity is inversely proportional to ν, in agreement with [64, 84]. Note that $\nu = 0$ was employed in the NSTX analysis, but finite ν was required to provide a reasonable description of the C-Mod data.

Appendix B. The Reynolds stress proxy (RSP)

The idea and central assumption behind the RSP is that the eddy structures of electrostatic potential have the same shape and orientation as the GPI images. Under this assumption, is it possible to form the Reynolds stress $\langle v_x v_y \rangle$ from the elliptical equipotential flow contours and average it around the ellipse to obtain a proxy for the Reynolds stress.

Let

$$\Phi = \Phi(g) \tag{B1}$$

where

$$\frac{\xi^2}{r_1^2} + \frac{\eta^2}{r_2^2} = g^2 \tag{B2}$$

and the rotated coordinates ξ and η are defined by the r_1 and r_2 directions in figure 11(*a*) so that

$$\xi = x \cos(\hat{\theta}) + y \sin(\hat{\theta}) \tag{B3}$$

$$\eta = y \cos(\hat{\theta}) - x \sin(\hat{\theta}) \tag{B4}$$

where, for convenience, we let $\hat{\theta} = -\theta$. The $E \times B$ velocities are

$$v_x = -\frac{\partial \Phi}{\partial y} \tag{B5}$$

$$v_y = \frac{\partial \Phi}{\partial x}. \tag{B6}$$

Therefore, using the chain rule, e.g.

$$\frac{\partial \Phi}{\partial x} = \frac{\mathrm{d}\Phi}{\mathrm{d}g} \frac{\partial g}{\partial x} = \frac{\mathrm{d}\Phi}{\mathrm{d}g} \left(\frac{\partial g}{\partial \xi} \frac{\partial \xi}{\partial x} + \frac{\partial g}{\partial \eta} \frac{\partial \eta}{\partial x} \right) \tag{B7}$$

with

$$\frac{\partial g}{\partial \xi} = \frac{\xi}{g r_1^2} \tag{B8}$$

$$\frac{\partial g}{\partial \eta} = \frac{\eta}{g r_2^2} \tag{B9}$$

one obtains

$$v_x = -\frac{1}{g} \frac{\mathrm{d}\Phi}{\mathrm{d}g} \left(\frac{\xi}{r_1^2} \sin \hat{\theta} + \frac{\eta}{r_2^2} \cos \hat{\theta} \right) \tag{B10}$$

$$v_y = \frac{1}{g} \frac{\mathrm{d}\Phi}{\mathrm{d}g} \left(\frac{\xi}{r_1^2} \cos \hat{\theta} - \frac{\eta}{r_2^2} \sin \hat{\theta} \right). \tag{B11}$$

The next step is to parametrize distance around the ellipse by an angle φ

$$\xi = g r_1 \cos \varphi \tag{B12}$$

$$\eta = g r_2 \sin \varphi \tag{B13}$$

so that

$$v_x = -\frac{\mathrm{d}\Phi}{\mathrm{d}g} \left(\frac{\cos \varphi \sin \hat{\theta}}{r_1} + \frac{\sin \varphi \cos \hat{\theta}}{r_2} \right) \tag{B14}$$

$$v_y = \frac{\mathrm{d}\Phi}{\mathrm{d}g} \left(\frac{\cos \varphi \cos \hat{\theta}}{r_1} - \frac{\sin \varphi \sin \hat{\theta}}{r_2} \right). \tag{B15}$$

We introduce the average over φ

$$\langle ... \rangle = \int \frac{\mathrm{d}\varphi}{2\pi} (...) \tag{B16}$$

to obtain

$$\langle v_x v_y \rangle = \frac{1}{4 r_2^2} \left(\frac{\mathrm{d}\Phi}{\mathrm{d}g} \right)^2 \sin 2\hat{\theta} \left(1 - \frac{r_2^2}{r_1^2} \right). \tag{B17}$$

Thus, an unnormalized proxy for the RS $\propto \langle v_x v_y \rangle$, in terms of the original angle θ, is

$$\mathrm{RSP} = -\sin 2\theta \left(1 - \frac{r_2^2}{r_1^2} \right). \tag{B18}$$

References

[1] Diamond P.H. *et al* 2005 *Plasma Phys. Control. Fusion* **47** R35
[2] Diamond P.H. and Kim Y.-B. 1991 *Fluids* B **3** 1626
[3] Terry P.W. 2000 *Rev. Mod. Phys.* **72** 109
[4] Scott B.D. 2005 *New J. Phys.* **7** 92
[5] Naulin V. *et al* 2005 *Phys. Plasmas* **12** 052515
[6] Krasheninnikov S.I. *et al* 2008 *J. Plasma Phys.* **74** 679
[7] D'Ippolito D.A. *et al* 2011 *Phys. Plasmas* **18** 060501
[8] Maqueda R.J. *et al* 2001 *Rev. Sci. Instrum.* **72** 931
[9] Zweben S.J. *et al* 2004 *Nucl. Fusion* **44** 134
[10] Terry J.L. *et al* 2003 *Phys. Plasmas* **10** 1739
[11] Kim E.J. and Diamond P.H. 2003 *Phys. Rev. Lett.* **90** 185006
[12] Malkov M.A. and Diamond P.H. 2009 *Phys. Plasmas* **16** 012504
[13] Delgado J.M., Garcia L. and Carreras B.A. 2009 *Plasma Phys. Control. Fusion* **51** 015003
[14] Zweben S.J. *et al* 2010 *Phys. Plasmas* **17** 102502
[15] Conway G.D. *et al* 2011 *Phys. Rev. Lett.* **106** 065001
[16] LaBombard B. *et al* 2005 *Phys. Plasmas* **12** 056111
[17] Schmitz L. *et al* 2012 *Phys. Rev. Lett.* **108** 155002
[18] Estrada T., Hidalgo C., Happel T. and Diamond P.H. 2011 *Phys. Rev. Lett.* **107** 245004
[19] Xu G.S. *et al* 2011 *Phys. Rev. Lett.* **107** 125001
[20] Tynan G.R. *et al* 2013 Power transfer to turbulent-driven low-frequency sheared $E \times B$ flows as the trigger for the H-mode *Nucl. Fusion* submitted
[21] Xu M. *et al* 2012 *Phys. Rev. Lett.* **108** 245001
[22] Lipschultz B. *et al* 2007 *Nucl. Fusion* **47** 1189
[23] Loarte A. *et al* 2007 Progress in the ITER Physics Basis, Chapter 4: Power and particle control *Nucl. Fusion* **47** S203
[24] Yu G.Q. and Krasheninnikov S.I. 2003 *Phys. Plasmas* **10** 4413
[25] Ghendrih Ph. *et al* 2003 *Nucl. Fusion* **43** 1013
[26] Myra J.R., D'Ippolito D.A., Krasheninnikov S.I. and Yu G.Q. 2004 *Phys. Plasmas* **11** 4267
[27] Xu G.S., Naulin V. and Fundamenski W. 2009 *Nucl. Fusion* **49** 092002
[28] Windisch T., Grulke O., Naulin V. and Klinger T. 2011 *Plasma Phys. Control. Fusion* **53** 124036
[29] Diallo A., Fasoli A., Furno I., Labit B., Podestà M. and Theiler C. 2008 *Phys. Rev. Lett.* **101** 115005
[30] Ricci P. and Rogers B.N. 2008 *Phys. Rev. Lett.* **100** 225002
[31] Sechrest Y. *et al* 2011 *Phys. Plasmas* **18** 012502
[32] Alonso J.A. *et al* 2012 *Nucl. Fusion* **52** 063010
[33] Alonso J.A. *et al* 2013 *Plasma Phys. Control. Fusion* **55** 014001
[34] Alonso J.A. *et al* 2006 *Plasma Phys. Control. Fusion* **48** B465
[35] Shesterikov I. *et al* 2012 *Nucl. Fusion* **52** 042004
[36] Fedorczak N. *et al* 2012 *Phys. Plasmas* **19** 072314
[37] Fedorczak N., Diamond P.H., Tynan G. and Manz P. 2012 *Nucl. Fusion* **52** 103013
[38] Xu X.Q. *et al* 2002 *New J. Phys.* **4** 53
[39] Ricci P. and Rogers B.N. 2013 *Phys. Plasmas* **20** 010702
[40] Terry J.L. *et al* 2009 *J. Nucl. Mater.* **390** 339
[41] Angus J.R., Krasheninnikov S.I. and Umansky M.V. 2012 *Phys. Plasmas* **19** 082312
[42] Zweben S.J. *et al* 2009 *Phys. Plasmas* **16** 082505
[43] Russell D.A., Myra J.R. and D'Ippolito D.A. 2009 *Phys. Plasmas* **16** 122304
[44] Garcia O.E. *et al* 2005 *Phys. Plasmas* **12** 062309
[45] Sarazin Y. and Ghendrih Ph. 1998 *Phys. Plasmas* **5** 4214
[46] Bisai N. *et al* 2005 *Phys. Plasmas* **12** 072520
[47] Garcia O.E. *et al* 2007 *Plasma Phys. Control. Fusion* **49** B47
[48] Russell D.A. *et al* 2011 *Phys. Plasmas* **18** 022306
[49] Myra J.R. *et al* 2011 *Phys. Plasmas* **18** 012305
[50] Russell D.A. *et al* 2012 *Phys. Plasmas* **19** 082311
[51] Fundamenski W. *et al* 2007 *Nucl. Fusion* **47** 417
[52] Militello F. *et al* 2013 *Plasma Phys. Control. Fusion* **55** 025005
[53] D'Ippolito D.A. *et al* 2012 *Phys. Plasmas* **19** 102301
[54] Davis W.M. *et al* 2012 *Bul. Am. Phys. Soc.* **57** 384
[55] Bisai N., Singh R. and Kaw P.K. 2012 *Phys. Plasmas* **19** 052509
[56] Furno I. *et al* 2011 *Plasma Phys. Control. Fusion* **53** 124016
[57] Braginskii S.I. 1965 *Rev. Plasma Phys.* vol 1 (New York: Consultants Bureau)
[58] Stangeby P.C. 2000 *The Plasma Boundary of Magnetic Fusion Devices* (Bristol: Institute of Physics Publishing)
[59] Cziegler I., Terry J.L., Hughes J.W. and LaBombard B. 2010 *Phys. Plasmas* **17** 056120
[60] Burrell K. 1997 *Phys. Plasmas* **4** 1499
[61] Agostini M. *et al* 2007 *Phys. Plasmas* **14** 102305
[62] Farina D. *et al* 1993 *Nucl. Fusion* **33** 1315
[63] Terry J.L. *et al* 2009 *J. Nucl. Mater* **390–391** 339
[64] Katz N. *et al* 2008 *Phys. Rev. Lett.* **101** 015003
[65] Cao B. *et al* 2012 *Plasma Phys. Control. Fusion* **54** 112001
[66] Russell D.A., Myra J.R. and D'Ippolito D.A. 2007 *Phys. Plasmas* **14** 102307
[67] Zweben S.J. *et al* 2012 *Plasma Phys. Control. Fusion* **54** 025008
[68] Bisai N. *et al* 2005 *Phys. Plasmas* **12** 102515
[69] Stotler D.P. *et al* 2004 *Contrib. Plasma Phys.* **44** 294
[70] Fujimoto T.J. 1979 *J. Quant. Spectrosc. Radiat. Transfer.* **21** 439
[71] Goto M.J. 2003 *J. Quant. Spectrosc. Radiat. Transfer.* **76** 331
[72] Zhang Y.Z., Xie T. and Mahajan S.M. 2012 *Phys. Plasmas* **19** 020701
[73] Manz P. *et al* 2012 *Phys. Plasmas* **19** 072311
[74] Myra J.R., Russell D.A. and D'Ippolito D.A. 2008 *Phys. Plasmas* **15** 032304
[75] Coppi B. *et al* 2006 *33rd EPS Conf. on Plasma Physics (Rome, 19–23 June 2006)* ECA vol 30I, O-4.017 http://epsppd.epfl.ch/Roma/pdf/O4_017.pdf
[76] Müller S.H. *et al* 2011 *Phys. Rev. Lett.* **106** 115001
[77] Xu G.S., Naulin V. and Fundamenski W. 2010 *Phys. Plasmas* **17** 022501
[78] Cohen R.H. and Ryutov D.D. 1997 *Nucl. Fusion* **37** 621
[79] Zweben S.J. *et al* 2012 *Plasma Phys. Control. Fusion* **54** 105012
[80] Theiler C. *et al* 2012 *Phys. Plasmas* **19** 082305
[81] LaBombard B. *et al* 2004 *Nucl. Fusion* **44** 1047
[82] Wakatani M. and Hasegawa A. 1984 *Phys. Fluids* **27** 611
[83] Ryutov D.D. 2006 *Phys. Plasmas* **13** 122307
[84] Kube R. and Garcia O.E. 2012 *Phys. Plasmas* **19** 042305